Monthly Notices
of the
ROYAL ASTRONOMICAL SOCIETY

MNRAS **502,** 5245–5258 (2021)
Advance Access publication 2021 February 11
doi:10.1093/mnras/stab369

Broad-band study of OQ 334 during its flaring state

Raj Prince ,[1★] Rukaiya Khatoon[2] and C. S. Stalin [3]
[1] *Center for Theoretical Physics, Polish Academy of Sciences, Al.Lotnikov 32/46, PL-02-668 Warsaw, Poland*
[2] *Tezpur University, Napaam 784028, Assam, India*
[3] *Indian Institute of Astrophysics, Block II, Koramangala, Bangalore 560034, India*

Accepted 2021 February 5. Received 2021 February 4; in original form 2020 October 22

ABSTRACT

The blazar OQ 334 displayed a γ-ray flare in 2018, after being in the long quiescent γ-ray state since 2008. Subsequent to the flare, the source was in a higher γ-ray flux state and again flared in 2020. We present here the first spectral and timing analysis of the source at its various flaring states. During the higher γ-ray state, we found four major peaks identified as P1, P2, P3, and P4. From timing analysis we found rise and decay time of the order of hours with the fastest variability time of 9.01 ± 0.78 h. We found the highest γ-ray photon of 77 GeV during P4, which suggests the location of the γ-ray emitting region at the outer edge of the broad line region or the inner edge of the torus. The γ-ray spectral analysis of the source indicates that during P4, the γ-ray spectrum clearly deviates from the power-law behaviour. From cross-correlation analysis of the γ-ray and radio light curves, we found that the two emission regions are separated by about 11 pc. Our broad-band spectral energy distribution modelling of the source during quiescent and active phases indicates that more electron and proton power are required to change the source from low flux to high flux state. The Anderson–Darling test and histogram fitting results suggest that the three days binned γ-ray fluxes follow a lognormal distribution.

Key words: galaxies: active – galaxies: individual: OQ334 – gamma rays: galaxies.

1 INTRODUCTION

Blazars are a peculiar category of active galactic nuclei (AGNs) that have their relativistic jets aligned close to the line of sight (angles less than ∼14°) to the observer (Urry & Padovani 1995). Their energy output dominated by non-thermal emission spans the complete accessible electromagnetic spectrum. Blazars are highly luminous, have powerful jets, powered by massive black holes (Lynden-Bell 1969) and dominate the extragalactic γ-ray sky (Hartman et al. 1999; Abdo et al. 2010). They show large amplitude flux variability in different wavelengths such as radio, infrared, optical, X-rays, and γ-rays on a range of time-scales from minutes to hours to several days (Heidt & Wagner 1996; Ulrich, Maraschi & Urry 1997) and in some cases to decades (Goyal et al. 2017, 2018; Goyal 2020); For a review see Hovatta & Lindfors (2019). The increased capability in the recent years to acquire near simultaneous observations over different wavelengths have led to the identification of complex variability patterns across wavelengths in blazars. There are instances when the variations in the low energy optical and high energy γ-rays are correlated and also instances where uncorrelated variations between optical and γ-rays are noticed (Chatterjee et al. 2012; Rajput et al. 2019; Rajput, Stalin & Sahayanathan 2020). Also, the short time-scale of variations now observed in blazars indicate that the variations we observe in them arise from very small regions in their jets.

The broad-band spectral energy distribution (SED) of blazars show two distinct humps. The low energy hump peaks in the UV/X-ray region and is now understood to be due to synchrotron emission from relativistic electrons in their jet. The high energy hump peaks in the MeV–GeV energy range and the physical mechanisms responsible for the high energy hump is still debated. In the widely used leptonic model of emission from blazar jets, the high energy emission is due to inverse Compton process. The seed photons for the inverse Compton process can be photons internal to the jet (synchrotron self-Compton; Sikora et al. 2009) or external to the jet (external compton; Dermer, Schlickeiser & Mastichiadis 1992; Sikora, Begelman & Rees 1994). Alternative to the leptonic process is the hadronic process. In this model, the high energy emission is explainable by proton synchrotron process or photopion process (B”ottcher et al. 2013). Thus, carrying out timing and SED analysis of blazars can provide valuable clues to the processes happening close to the central regions of blazars. In spite of such studies done on blazars, we yet do not have a clear understanding of the physical processes happening in blazar jets.

The observed broad-band SED of blazars is complex. For example, SED modelling of 3C 279 using the one zone leptonic emission model during the flares in 2017–2018, favours the γ-ray emission site to be located at the outer boundary of BLR (Prince 2020). Also, the flare of 2014 March in 3C 279 was not detected in the very high energy γ-ray band, and the Fermi observations were explained in the one-zone leptonic emission model with the requirement of seed photons for inverse Compton scattering from both the BLR and the torus (Paliya, Sahayanathan & Stalin 2015). Alternatively, during the epoch of the hard γ-ray flare from 3C 279 in 2013 December, the SED was fit by both lepto-hadronic model and two-zone leptonic model (Paliya et al. 2016). This clearly indicates that even in the same source, different radiative processes contribute at different epochs, reflecting the complexities seen in emission from blazar jets. In another FSRQ, Ton 599, the γ-ray emission site is found to be at the outer edge of

---

★ E-mail: raj@cft.edu.pl

Published by Oxford University Press on behalf of Royal Astronomical Society

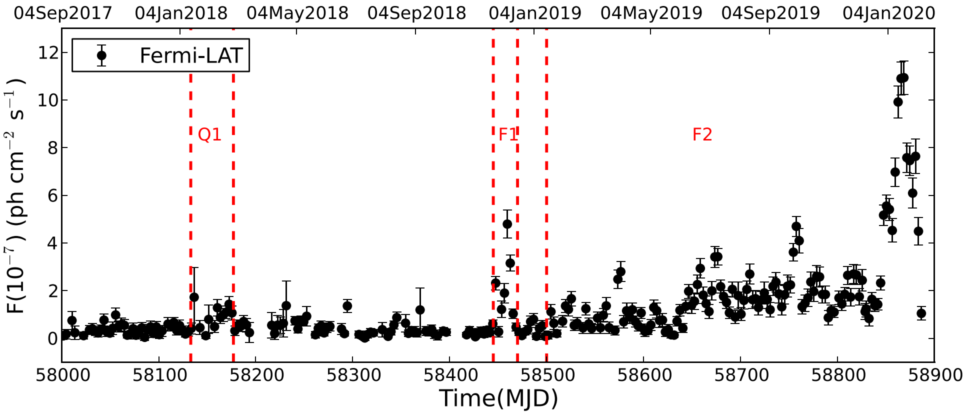

Figure 1. The long-term γ-ray light curve of OQ 334. State Q1 represents the quiescent state, and F1 and F2 are the two flaring states.

the BLR (Prince 2019) based on leptonic model fit to the observed SED. Recently, the SED of the BL Lac Mrk 421 was found to be equally fit by all the models such as leptonic, hadronic, and lepto-hadronic (Cerruti 2020). In the source Cen A, there are reports that the obsevations are fit by proton-synchrotron model (Banik, Bhadra & Bhattacharyya 2020). Also, the recent detection of neutrions from the blazar TXS 0506+056 (IceCube Collaboration 2018) seems to favour lepto-hadronic over leptonic models (Cerruti et al. 2019). It is believed that γ-ray flares without counterparts in the optical band cannot be explained in the one-zone leptonic emission sceanrio and could favour hadronic models. Indeed, from analysis of a sample of FSRQs, Rajput et al. (2019, 2020) have found that in a source there are epochs when there are optical flares without gamma-ray flares, gamma-ray flares without optical counterparts and correlated optical and γ-ray flares, all of which are explainable in the leptonic scenario. Thus, recent observations on a handful of blazars clearly indicate that the exact reasons for the origin of high energy emission in blazar is complex, still not understood and possibly future X-ray polarization observations could provide the needed observational constrains on the high energy emission process in blazars. Given the current scenario, it is of utmost importance to carry out timing and SED analysis of more and more number of blazars.

The blazar OQ 334 is classified as a flat spectrum quasar (FSRQ) in 4FGL (Abdollahi et al. 2020) and it is at a redshift z = 0.6819 (Hewett & Wild 2010). It has been in the low γ-ray brightness state since 2008. After a decade it flared in the γ-ray band in 2018 (Ciprini 2018). Subsequently, it was in a higher γ-ray brightness state and again flared in the γ-ray band in 2020 (Ciprini & Cheung 2020). Observations were also available in the X-ray and optical/UV bands during the flaring epochs of the blazar from *Swift*. This source has not yet been studied for its γ-ray characteristics, however reports on its γ-ray flaring are available (Ciprini 2018; Angioni 2019; Ciprini & Cheung 2020). Therefore, in this work we carried out detailed timing and spectral analysis of the source during both its flaring periods as well as a quiescent period.

This paper is organized as follows. In Section 2, we describe the mulitwavelength data and reduction, the results are shown in Sections 3, 4, and 5, followed by the summary in the final Section.

2 MULTIWAVELENGTH OBSERVATIONS AND DATA ANALYSIS

The FSRQ OQ 334 was found to show two episodes of flaring, one in 2018 and the other in 2020, based on observations with the Large Area Telescope on board the *Fermi* Gamma-ray Space Telescope. To understand the nature of the source during its high activity states relative to its quiescent state necessitates creation of broad-band SED, which in turn requires data at other wavelengths also. Towards this we looked into the γ-ray data from *Fermi–LAT*, X-ray from *Swift–XRT*, and Ultraviolet and optical data from *Swift–UVOT*.

2.1 *Fermi*–LAT

Fermi–LAT observes the galactic as well as the extragalactic sky in γ-ray. It is based on the pair conversion method, and the working energy range is 20 MeV–500 GeV. It has a vast field of view (FoV) of about 2.4 sr (Atwood et al. 2009), which scans 20 per cent of the sky at any time. The total scanning period of the entire sky is around three hours. *Fermi*–LAT is continuously monitoring the source OQ 334/B2 1420+32 since 2008. LAT data in the energy range 100 MeV to 300 GeV were taken for the period 2008 December to 2020 February. We followed the standard procedure for the reduction of γ-ray data as given in Science Tools.[1] More details about the reduction can be found in Prince et al. (2018). We generated 3 d bin light curve covering a duration of 900 d from MJD 58000 to MJD 58900. This is shown in Fig. 1. Each points in the light curve pertains to a test statistics (TS) greater than 9, which corresponds to a 3σ detection.

2.2 *Swift*–XRT/UVOT

2.2.1 *X-ray*

The X-ray data used in this work is from *Swift/XRT* in the energy range of 0.3–10 keV. X-ray data from *Swift* was not available for most of the duration of the γ-ray light curve, however sparsely available during the two flaring periods of OQ 334. The log of the X-ray observations used in this work is given in Table 1. For all the observations given in Table 1, we used the task XRTPIPELINE to generate clean event files. We used the CALDB version 20160609 for *Swift–XRT* analysis. The clean event files were further processed using XSELECT in Xspec (Arnaud 1996). The events from the source were selected from a circular region of radius 12 arcsec. The background was selected from a region of similar size but away from the source. We modelled the generated spectra using the simple power-law model F(E) $\propto$ E$^{\Gamma}$. For spectral fit we binned

---

[1] https://fermi.gsfc.nasa.gov/ssc/data/analysis/documentation/

Table 1. Log of the *Swift* observations during all the states (Q1, F1, and P4).

Observatory	Obs-ID	Exposure (ks)
Q1		
Swift–XRT/UVOT	00010520001	1.0
Swift–XRT/UVOT	00010520002	2.9
F1		
Swift–XRT/UVOT	00010520004	1.8
Swift–XRT/UVOT	00010520005	2.1
Swift–XRT/UVOT	00010520006	1.9
P4		
Swift–XRT/UVOT	00010520014	2.5
Swift–XRT/UVOT	00010520015	1.6
Swift–XRT/UVOT	00010520016	1.9
Swift–XRT/UVOT	00010520017	2.0
Swift–XRT/UVOT	00010520018	1.6
Swift–XRT/UVOT	00010520019	1.5
Swift–XRT/UVOT	00010520022	1.8
Swift–XRT/UVOT	00010520024	1.8
Swift–XRT/UVOT	00010520025	1.8
Swift–XRT/UVOT	00010520026	2.0
Swift–XRT/UVOT	00010520027	1.2
Swift–XRT/UVOT	00010520028	1.7
Swift–XRT/UVOT	00010520029	2.0
Swift–XRT/UVOT	00010520030	2.4

the data to have a minimum of 20 counts per bin. For the power-law fit, we used a fixed galactic absorption column density $n_H = 1.10 \times 10^{20}\,\mathrm{cm}^{-2}$ taken from Kalberla et al. (2005). We generated the spectrum file for each observations and if in a particular flaring period we have more than one observations, we combined the spectra in ADDSPEC.[2] In ADDSPEC, we added the source spectra along with the redistribution matrix files (RMF) and the ancillary response files (ARF) for different observations. Similarly, the background spectra from different observations were added in MATHPHA.[3] The combined X-ray spectrum from each period (quiescent-sate, flare-1, and P4) was finally used in the multiwavelength SED modelling.

2.2.2 *UV and optical*

In the optical and ultraviolet (UV) bands, we used data from the *Swift–UVOT* (Roming et al. 2005) in the filters *U*, *B*, *V*, *W1*, and *W2*. For each of these filters, we added the observations accumulated over a given period using the task UVOTIMSUM and we derived the magnitude of the target blazar using UVOTSOURCE. We corrected the magnitudes for galactic extinction following Schlafly & Finkbeiner (2011) and converted the extinction-corrected magnitudes to fluxes using the zero points (Breeveld et al. 2011) and conversion factors given in Larionov et al. (2016).

2.3 Radio data at 15 GHz

In the radio band we used the data at 15 GHz from the Owens Valley Radio Observatory (OVRO; Richards et al. 2011). The blazar OQ 334 is part of the OVRO monitoring program and therefore data at 15 GHz with a time resolution of about 2 weeks is available for most of the duration of the γ-ray light curves.

3 RESULTS: TEMPORAL AND SPECTRAL ANALYSIS

A detailed temporal and spectral study has been done using the multiwavelength data from the *Fermi*–LAT, and the *Swift–XRT/UVOT* telescope. The archival data from OVRO is used to perform the correlation study with the γ-ray to examine the possible location of their emission regions.

3.1 γ-ray flux variability

We show in Fig. 1 the three day binned γ-ray light curve of OQ 334. As can be seen, the source was in a low γ-ray brightness state till 2018, when it first showed a γ-ray flare with a three day binned γ-ray flux of 4.79 ± 0.59 ($\times 10^{-7}\,\mathrm{ph\,cm^{-2}\,s^{-1}}$) and an average γ-ray photon index of 1.96 ± 0.10, this has also been reported in Ciprini (2018) and shown in Fig. 1 as F1 (Flare-1). The source remained in the low brightness state for a few days after the flare and then it showed a steady increase in the γ-ray brightness level. Superimposed on the high γ-ray brightness level, we noticed several flares that also includes a major flare in early 2020. From the three day binned light curve, we identified three major regions, a quiescent state Q1, a flaring state F1, and a higher brightness state F2. The higher brightness state was further divided into pre-flare (MJD 58500–58631) and flaring period (MJD 58631–58887), based on the average flux seen in the 3 d binned γ-ray light curve (Fig. 2). For pre-flare and flare periods we found average flux values of 6.09 ± 0.36 ($\times 10^{-8}$ and 1.72 ± 0.03 ($\times 10^{-7}\,\mathrm{ph\,cm^{-2}\,s^{-1}}$), respectively. To substantiate this division based on the mean flux values, we also calculated the fractional flux variability (F_{Var}; Prince et al. 2018). We found F_{Var} values of 0.61 ± 0.05 and 0.81 ± 0.02, for the pre-flare and flare periods, respectively.

To further characterize the flux variability pattern in the flaring period, we generated 1 d binned γ-ray light curve. From this 1 d binned light curve, we identified four high flux states (with flux exceeding $\sim 4 \times 10^{-7}\,\mathrm{ph\,cm^{-2}\,s^{-1}}$) denoted as P1, P2, P3, and P4. The colour patches in Fig. 2 denote the total duration of each of these flux states. The details about all the states and their periods are mentioned in Table 2. Further, we also generated 12 h binned γ-ray light curve to model the variations in the high flux states with a sum of exponential functions. This function is used to estimate the rising and decaying time of the peaks observed within the high state periods. The functional form of the sum of exponentials is given below,

$$F(t) = 2F_0 \left[\exp\left(\frac{t_0 - t}{T_{\mathrm{r}}}\right) + \exp\left(\frac{t - t_0}{T_{\mathrm{d}}}\right) \right]^{-1}, \qquad (1)$$

where T_{r} and T_{d} are the rise and decay times of the peaks, respectively, and the peak amplitude is approximated as F_0 measured at time t_0. The fits to the light curve for all the high states (P1, P2, P3, and P4) are shown in Fig. 3, and the corresponding fitted parameters are given in Table 3. Various peaks observed in the high states P1, P2, P3, and P4 in Fig. 3 from left to right are denoted in the serial number (1, 2, 3,..etc.) in Table 3. The temporal fitting for the high states P1, P2, and P3 was done for the 12 h binned light curve. However, in the case of high state P4, the 12 h binned light curve has large error bars, and hence we considered the one-day binned light curve for temporal study. For the first three cases, we also considered the constant flux state (shown in grey) while doing the temporal fitting, which shows the flux level before and after the peaks.

---

[2] https://heasarc.gsfc.nasa.gov/ftools/caldb/help/addspec.txt

[3] https://heasarc.gsfc.nasa.gov/ftools/caldb/help/mathpha.txt

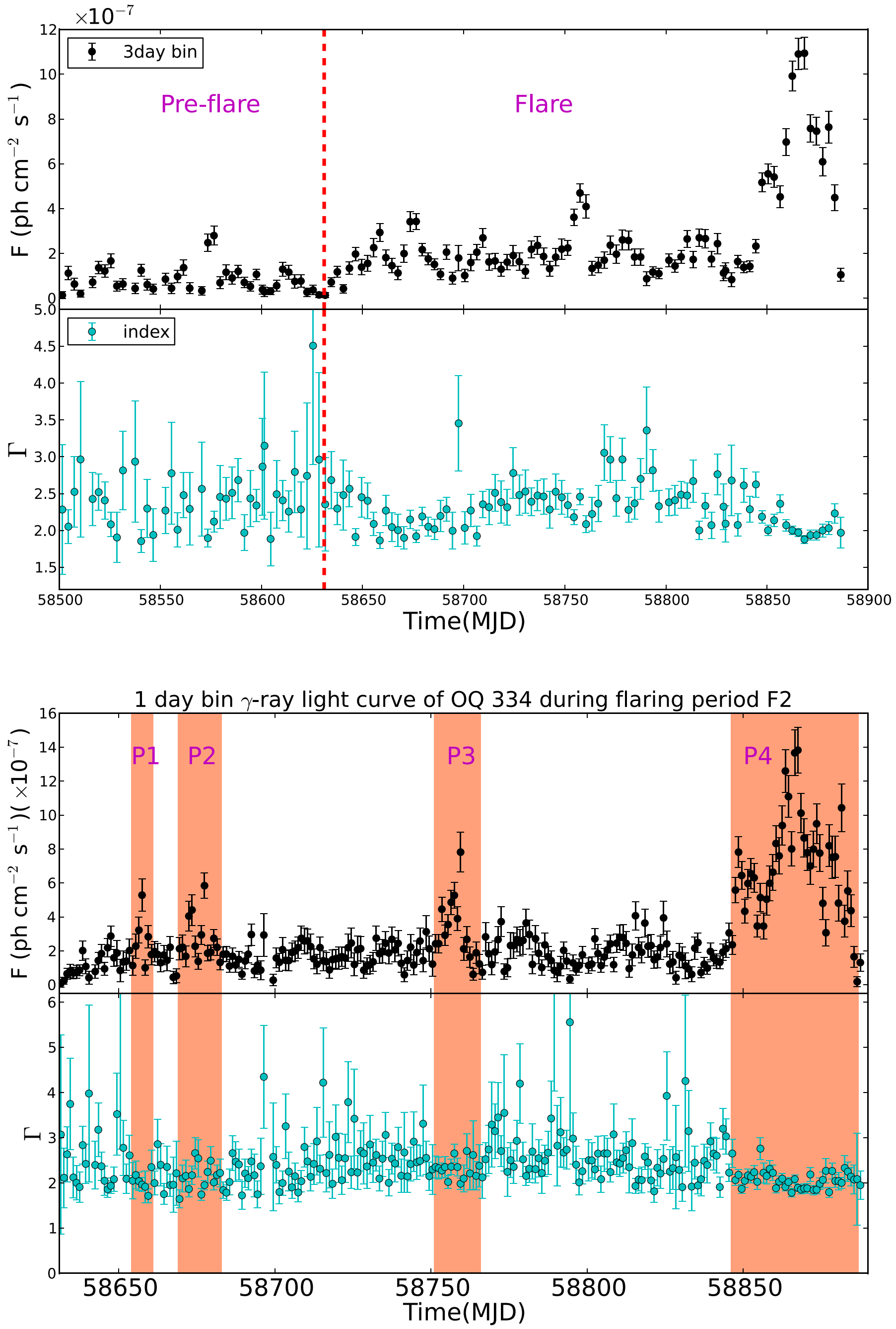

Figure 2. The upper plot shows the γ-ray light curve of state F2 with the spectral index, divided into pre-flare and flare. The lower plot is the one-day binned γ-ray light curve of the flaring period. The colour patches describe the various peaks observed in the flaring part.

Table 2. Details about the various states recognized in this study.

States	MJD start	MJD end	Duration (d)
Q1	58133	58177	44
F1	58445	58470	25
F2/pre-flare	58500	58631	131
F2/ flare	58631	58887	256
P1	58654	58661	7
P2	58669	58683	14
P3	58751	58766	15
P4	58846	58887	41

3.1.1 *Spectral variations*

A harder when brighter trend is generally seen in the high energy γ-ray emission from blazars (Ton 599; Prince 2019, 3C 279; Prince 2020). To investigate spectral variations if any, we show in Fig. 4, the variation of Γ with the observed γ-ray brightness during the states P1, P2, P3, and P4. We did not find any significant spectral variations with brightness.

3.2 Highest energy photon

In the FSRQ category of AGN, detection of γ-ray photons with energy >20 GeV (Liu & Bai 2006) suggests the location of the γ-

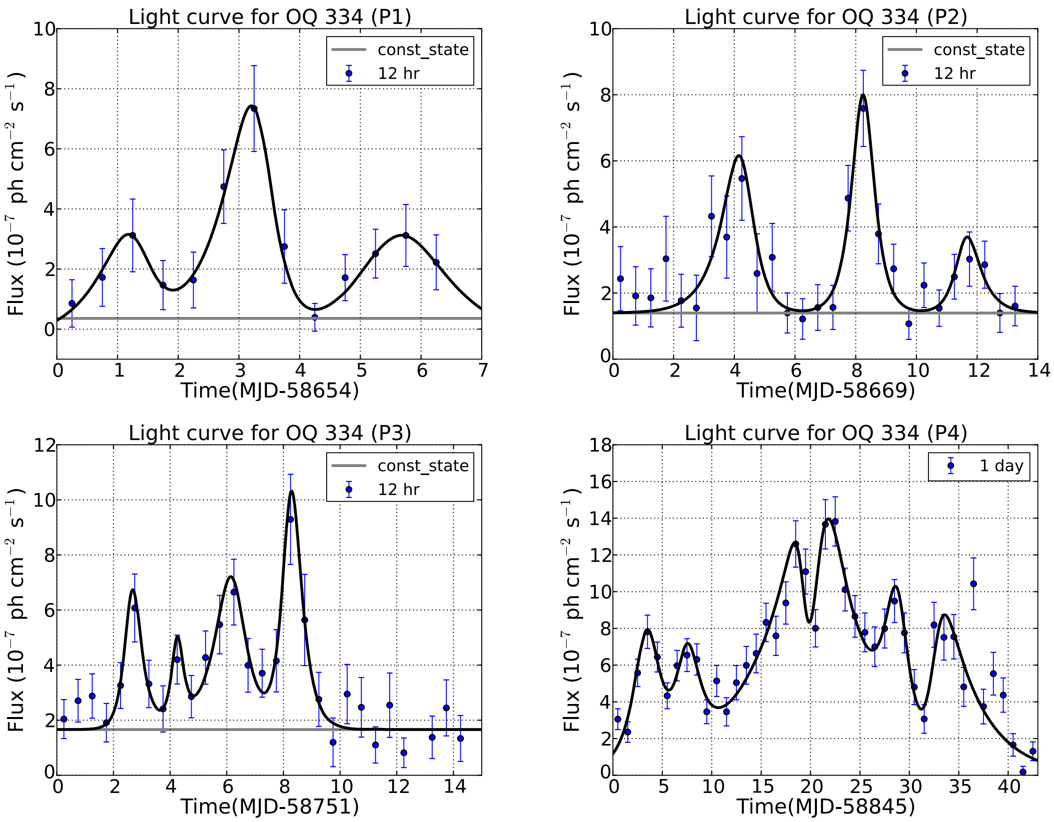

Figure 3. Light-curve fitting of different flares observed in OQ 334.

Table 3. The rise and decay times estimated from equation (1) for all the peaks. The peak flux F$_0$ is in units of ($\times 10^{-7}$) ph cm^{-2} s^{-1}.

Peaks	t_0 (MJD)	F_0	T_r (h)	T_d (h)
P1				
1	58655.25	3.12 ± 1.21	13.93 ± 2.99	6.22 ± 1.76
2	58657.25	7.34 ± 1.43	13.67 ± 1.47	5.56 ± 0.78
3	58659.25	3.12 ± 1.03	14.90 ± 3.35	17.69 ± 5.20
P2				
1	58673.25	5.46 ± 1.26	14.51 ± 3.43	8.48 ± 2.75
2	58677.25	7.59 ± 1.15	8.13 ± 1.46	7.76 ± 1.40
3	58680.75	3.03 ± 0.82	7.05 ± 2.96	10.77 ± 4.05
P3				
1	58753.75	6.07 ± 1.23	6.73 ± 1.92	8.51 ± 2.93
2	58755.25	4.20 ± 0.88	4.70 ± 4.34	4.85 ± 4.32
3	58757.25	6.65 ± 1.19	15.03 ± 4.07	11.78 ± 3.58
4	58759.25	9.29 ± 1.63	6.72 ± 2.01	9.34 ± 2.12
P4				
1	58848.50	7.81 ± 0.90	29.12 ± 5.03	26.49 ± 11.93
2	58852.50	6.54 ± 0.89	23.66 ± 15.68	27.33 ± 9.80
3	58863.50	12.60 ± 1.26	125.17 ± 15.19	10.69 ± 4.67
4	58867.50	13.82 ± 1.34	18.87 ± 5.01	90.34 ± 14.66
5	58873.50	9.49 ± 1.17	27.75 ± 12.08	22.65 ± 9.50
6	58877.50	8.19 ± 1.23	15.15 ± 7.67	88.66 ± 10.45

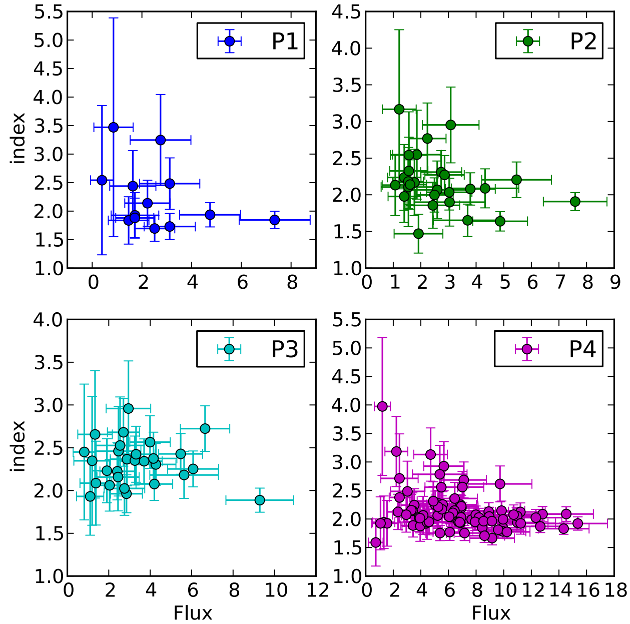

Figure 4. The γ-ray photon spectral index of all high states from 12 h bin light curve, with respect to the observed flux. The brighter-when-harder behaviour is not much clear in this case unlike most of the FSRQ type blazar .

ray emission region outside the broad-line region (BLR). In such instances, the high energy photons, in the leptonic scenario are the result of inverse Compton scattering of photons from the dusty torus by the relativistic electrons in the jet. We estimated the number of high energy photons during the higher brightness state of the source and this is shown in Fig. 5. We found two instances when γ-ray photons of energy >70 GeV with the probability of being from the

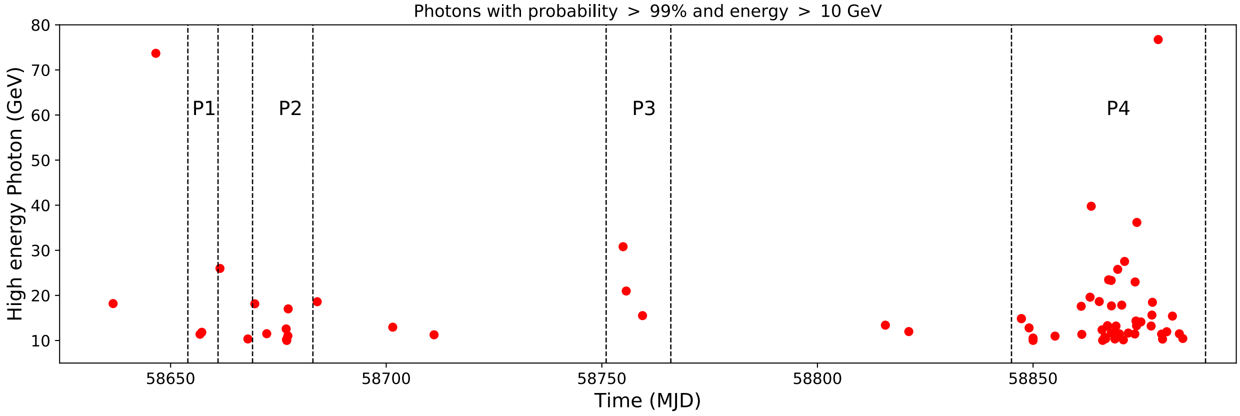

Figure 5. The arrival of high energy photon with probability >99 per cent for being from the source are shown here. We have considered photons of energy greater than 10 GeV.

source is greater than 99 per cent. By comparing Fig. 5 with the light curve shown in Fig. 2, we conclude that the photon with energy ∼72 GeV was detected just before the high state P1, while the photon of energy ∼77 GeV was detected during P4. Detection of such high energy photons point to the location of the γ-ray emission site just at the boundary of BLR or the inner edge of the torus during P4.

3.3 γ-ray spectra

We generated the γ-ray spectrum for all the states identified in Figs 1 and 2. The spectra were created using *likeSED.py* a python code provided by *Fermi* Science Tools. We carried out likelihood analysis on the spectral data points using power law (PL), log parabola (LP), broken power law (BPL), and power law with exponential cut-off (PELC) models. The γ-ray spectra along with the model fits are shown in Fig. 6 and the corresponding best-fitting model parameters are given in Table 4. We calculated $\mathrm{TS_{curve}} = 2(\log \mathrm{L(LP/BPL/PLEC)} - \log \mathrm{L(PL)})$, where L represents the likelihood function (Nolan et al. 2012), to arrive at the suitability of the LP, BPL, and PLEC models over the PL model to describe the data. The best spectral model favours a value larger than $\mathrm{TS_{curve}} = 16$ which is significant at the 4 sigma level (Mattox et al. 1996).

The $\mathrm{TS_{curve}}$ reveals presence of curvature or break in the spectrum, and which could be caused by the absorption of high energy photons (>20 GeV; Liu & Bai 2006) by the BLR assuming the emitting region is located within the BLR. However, if the emitting region is located outside the BLR a nice power-law spectral behaviour is expected.

The various models and their corresponding parameters are shown in Table 4. The states, Q1, F1, pre-flare, P1, P2, P3, and P4 prefer models deviant from PL behaviour. The states where the PLEC best fits the spectra appears to have similar cut-off energy between 20 and 30 GeV, which is also the cut-off put by γ–γ absorption (Liu & Bai 2006) within the BLR, and hence it is likely that the γ-ray emission region associated with these states is present at the outer boundary of the BLR. However, a recent study of 106 FSRQs by Costamante et al. (2018) suggests that the smooth cut-off seen in the γ-ray spectrum between a few GeV to a few tens GeV is most probably the result of the end of the accelerated particle distribution.

The PL photon spectral index suggests a significant spectral hardening as the source transits from pre-flare to flare state (P1, P2, P3, and P4) and it is also true when the source changes from state Q1 to F1. The cut-off energy (E_{cutoff}) in the PLEC model is different for different flaring states and this is compatible with the detection of high energy photons in various states (Fig. 5). So, E_{cutoff} for P1, P2, P3, and P4 are ∼10, ∼20, ∼24, and ∼28 GeV, and comparing these values to that in Fig. 5 suggests that no high photons greater than these energies are detected in all the various states except P4. A high energy photon of energy greater than 70 GeV is found during P4, which suggests that this photon might be produced at the boundary or beyond the BLR. The BPL fit to the spectrum reveals that the break energy (E_{break}) is almost constant (at ∼1 GeV) for all the various states, and which could be seen as the reflection of emitting electrons distribution. However, the break in BPL during state Q1 and F1 is different from all the other states which probably suggests the involvement of different emission regions.

3.4 Correlations studies

To investigate correlation, if any, between flux variations in the γ-ray band and other wavelengths, we looked into the archives for the availability of data at multiple wavelengths. We could find data only in the radio band at 15 GHz that overlaps with the γ-ray light curve. The site of γ-ray production in blazars is controversial. Some study suggests that γ-rays are generally produced at the sub-parsec scale from the apex of the jet (Dermer & Schlickeiser 1994; Blandford & Levinson 1995; Ghisellini & Madau 1996). The radio core, which is the source of radio emission in the jet represents a transition zone from synchrotron self-absorbed region to optically thin region (Blandford & Königl 1979). It is also believed that the radio core is generally located at pc scales from the central super massive black hole (SMBH). Correlation between γ and radio light curves will help one to constrain the location of these emission regions. The long-term radio and γ-ray light curves are shown in Fig. 7. From Fig. 7, it is evident that flux variations in the γ-ray band is more compared to the radio band that suggest that γ-rays are produced close to the base of the jet, while, the radio emission is produced at much farther distance from the SMBH. We correlated the γ-ray and radio light curves for a bin size of 20 d using the discrete correlation function method of Edelson & Krolik (1988). The correlation function is shown in Fig. 8. We found a strong correlation with the correlation coefficient greater than 70 per cent with the radio emission leading the γ-ray emission by 70 d. This suggests that the γ-ray and radio emissions are produced at different locations along the jet axis. Similar result on radio leading the γ-ray flux variations is also seen in the blazar 3C

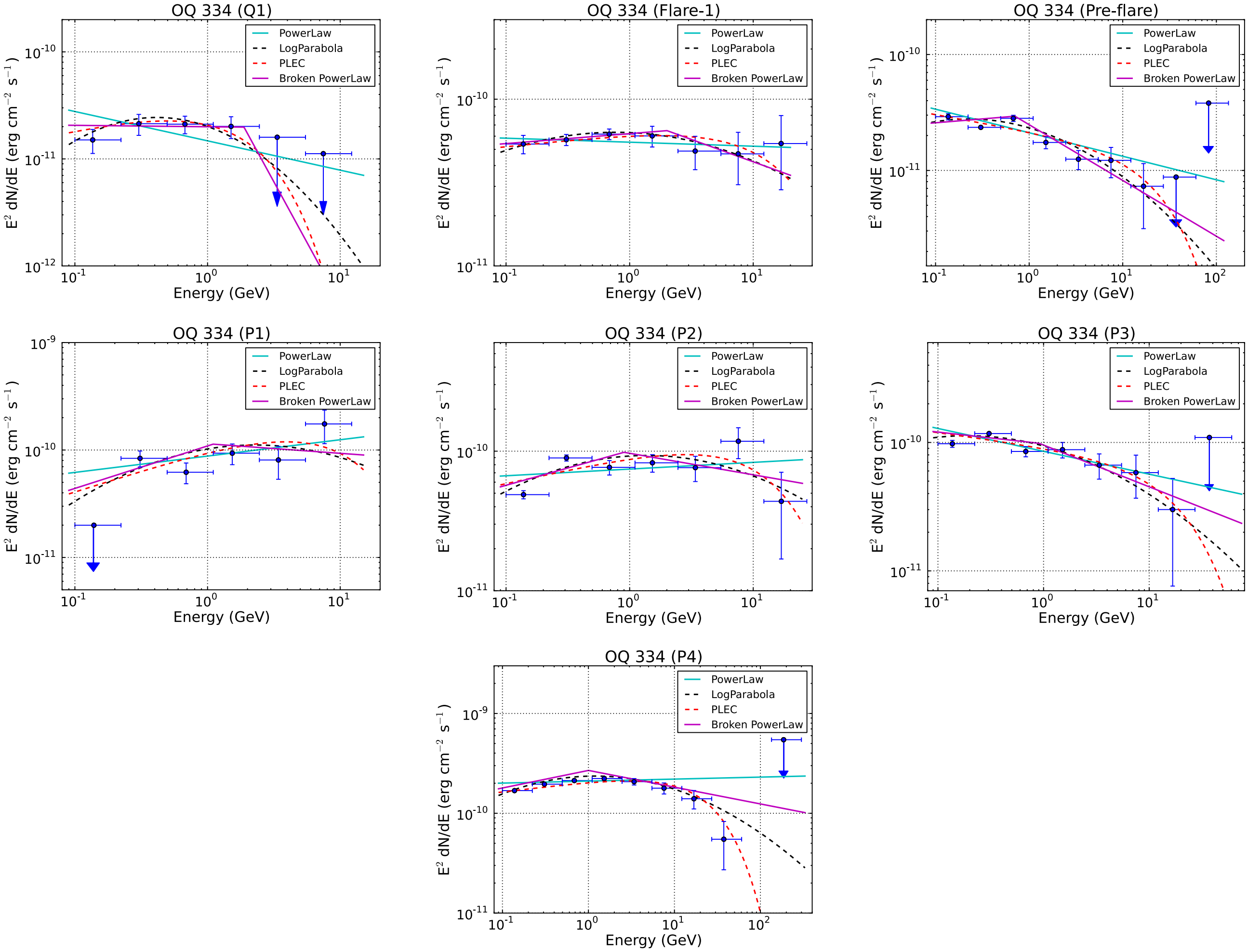

Figure 6. γ-ray spectral energy distributions (SED) for all the four flaring states and one long pre-flare state along with state Q1 and F1. Four different spectral models are used to fit the spectrum.

84, where Britzen et al. (2019) found the radio emission to lead the γ-ray emission by 300–400 d. From the observed time lag, following Prince (2019) we estimated the separation between γ-ray and radio emission as 11 pc along the jet axis for an average $\beta_{\rm app}$ value of 13.98 and a θ of 4.2° (Liodakis et al. 2017).

We also estimated the significance of the DCF peaks observed in cross-correlation. For that, we simulated 1000 γ-ray light curves by following the method mentioned in Emmanoulopoulos, McHardy & Papadakis (2013) and incorporated into a code by Connolly (2016) and available for use.[4] For simulating the γ-ray light curves we used power law as the shape of the power spectral densities (PSD; slope = 1.5) and assumed a lognormal form for the probability density function. This agrees well with the observations as the observed flux distribution also has a lognormal shape. We also simulated the radio light curve with PSD power-law slope 2.0 as suggested by Max-Moerbeck et al. (2014) for the significance estimation. Further, the simulated γ-ray light curves are cross-correlated with the simulated radio light curve. A 2σ and 3σ significance for each time lag was estimated and plotted horizontally in cyan and green yellow colour in Fig. 8.

3.5 Multiwavelength light curves

We also looked for the availability of multiwavelength (MW) data for this source along with the *Fermi*–LAT, but apparently, no multiwavelength observations are available for the pre-flare and flare state except state P4. Therefore, we collected the observations from the *Swift–XRT/UVOT* and analysed the X-ray and UV/optical data. Though we do not have a good number of observations in X-ray and UV/optical, the corresponding multiwavelength light curve for P4 is shown in Fig. 9. The significant peaks observed in γ-ray around MJD 58865 seem missing in X-ray and UV/optical because of the unavailability of observational data. The observation before MJD 58865 in X-ray and UV/optical light curve seems to peak around MJD 58865, and the observation after MJD 58865 suggests the decay in the flux after MJD 58865. Because of the highly sparsed data in X-ray and UV/optical, we could not do correlation and the time variability studies.

We calculated the fastest γ-ray variability time-scale during the flaring states of the source using

$$F_2 = F_1.2^{(t_2-t_1)/\tau_d}, \quad (2)$$

where F_1 and F_2 are the fluxes at consecutive times t_1 and t_2, respectively and $\tau_{\rm d}$ is the flux doubling time also known as variability

---

[4] https://github.com/samconnolly/DELightcurveSimulation

Table 4. Results of γ-ray SED analysis for various observed states.

Various states	$F_{0.1-300\mathrm{GeV}}$ (10^{-7} ph cm^{-2} s^{-1})	Luminosity (10^{48} erg s^{-1})	Power law Γ			−log(Likelihood)	TS_{curve}
Q1	1.42 ± 0.18	0.15	− 2.27 ± 0.09	–	–	24756.95	–
F1	3.46 ± 0.21	0.60	− 2.02 ± 0.04	–	–	40874.32	–
Preflare	1.61 ± 0.08	0.25	− 2.20 ± 0.03	–	–	207593.05	–
P1	3.87 ± 0.42	0.80	− 1.85 ± 0.07	–	–	11168.86	–
P2	4.72 ± 0.27	0.93	− 1.95 ± 0.04	–	–	32409.23	–
P3	7.02 ± 0.35	1.04	− 2.18 ± 0.04	–	–	35172.62	–
P4	12.00 ± 0.28	2.92	− 1.98 ± 0.02	–	–	103977.92	–
			LogParabola α	β			
Q1	1.14 ± 0.20	0.14	2.25 ± 0.13	0.25 ± 0.11	–	24752.63	8.64
F1	3.30 ± 0.22	0.60	1.98 ± 0.05	0.06 ± 0.03	–	40868.08	12.48
Preflare	1.50 ± 0.09	0.22	2.18 ± 0.07	0.04 ± 0.03	–	207588.33	9.44
P1	3.37 ± 0.42	0.81	1.70 ± 0.10	0.12 ± 0.05	–	11165.35	7.02
P2	4.37 ± 0.28	0.84	1.74 ± 0.08	0.08 ± 0.03	–	32400.11	18.24
P3	6.77 ± 0.36	0.96	2.06 ± 0.07	0.07 ± 0.03	–	35169.75	5.74
P4	11.20 ± 0.32	2.45	1.92 ± 0.02	0.06 ± 0.01	–	103956.66	42.52
			PLExpCutoff Γ_{PLEC}	E_{cutoff} (GeV)			
Q1	1.18 ± 0.20	0.14	− 1.71 ± 0.27	1.73 ± 0.91	–	24752.13	9.64
F1	3.31 ± 0.23	0.60	− 1.92 ± 0.07	22.02 ± 13.22	–	22397.94	36952.76
Preflare	1.57 ± 0.08	0.24	− 2.14 ± 0.04	29.72 ± 5.63	–	135578.86	144028.38
P1	3.50 ± 0.42	0.85	− 1.60 ± 0.13	9.77 ± 5.32	–	11164.87	7.98
P2	4.89 ± 0.28	1.20	− 1.88 ± 0.06	19.17 ± 9.70	–	32399.41	19.64
P3	6.90 ± 0.36	1.00	− 2.11 ± 0.06	23.80 ± 16.81	–	35170.84	3.56
P4	11.50 ± 0.29	2.54	− 1.89 ± 0.02	28.09 ± 6.46	–	77860.30	52235.24
			Broken power law Γ_1	Γ_2	E_{break} (GeV)		
Q1	1.23 ± 0.19	0.15	− 2.01 ± 0.14	− 4.27 ± 1.08	1.88 ± 0.09	24751.87	10.16
F1	3.35 ± 0.22	0.59	− 1.94 ± 0.06	− 2.27 ± 0.15	1.99 ± 0.00	40867.83	12.98
Preflare	1.47 ± 0.25	0.21	− 1.93 ± 0.25	− 2.48 ± 0.12	0.70 ± 0.17	207584.79	16.52
P1	3.52 ± 0.44	1.03	− 1.60 ± 0.19	− 2.09 ± 0.18	1.10 ± 0.75	11166.94	3.84
P2	4.43 ± 0.42	1.08	− 1.75 ± 0.14	− 2.15 ± 0.11	0.89 ± 0.29	32401.65	15.16
P3	6.86 ± 0.36	1.16	− 2.09 ± 0.09	− 2.32 ± 0.15	0.90 ± 0.95	35172.32	0.60
P4	11.30 ± 0.31	3.02	− 1.82 ± 0.04	− 2.17 ± 0.05	1.00 ± 0.22	103959.84	36.16

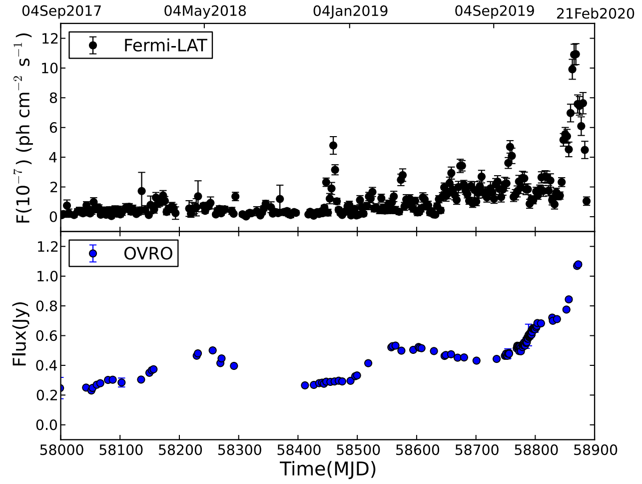

Figure 7. The long-term γ-ray and radio light curve used for correlation study.

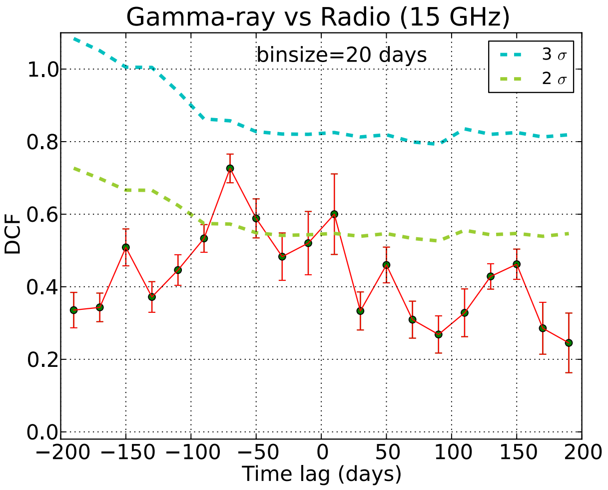

Figure 8. Cross-correlation of γ-ray and radio emission.

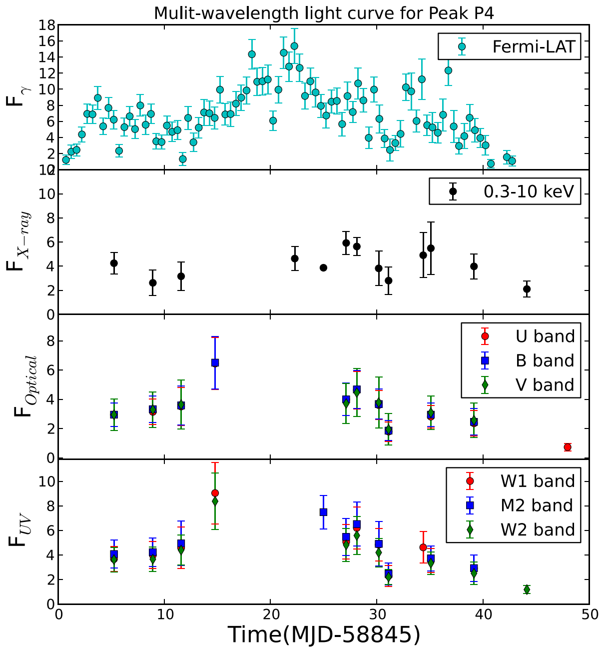

Figure 9. Multiwavelength light curves of P4. F_γ is in units of 10^{-7} ph cm^{-2} s^{-1}, $F_{\text{X-ray}}$ has unit of 10^{-12} erg cm^{-2} s^{-1}, and F_{optical} and F_{UV} is in units of 10^{-11} erg cm^{-2} s^{-1}.

time. We found the fastest variability time during P4 with a value of 9.01 ± 0.78 h between MJD 58874.25 and 58874.75, during which time the fluxes are 3.95 and 9.95 ($\times 10^{-7}$ ph cm^{-2} s^{-1}), respectively.

We also looked for the *Swift–XRT/UVOT* observations for the state Q1 and F1, and we found only few observations (hence the multiwavelength light curvs are not shown for Q1 and F1). The X-ray and optical/UV SED was prepared from that for both the states and used in the final MW spectral energy distribution (SED) modelling in the next section.

4 RESULTS: BROAD-BAND SED MODELLING

Fitting the observed SED of the source during various activity states is an ideal way to constrain the physical processes responsible for the broad-band emission. Towards this, we looked at the availability of multiband data covering UV, optical, and X-rays during the various activity periods of the source marked in Fig. 1. Multiwavelength data was sparsely available only for Q, F1, and P4 states. The multiwavelength light curves for the state P4 is shown in Fig. 9. Here too, X-ray and UV/optical observations are not available during the peak of the γ-ray flares. We modelled the observed SEDs during Q, F1, and P4 states using the python based and publicly available time-dependent model GAMERA[5] (Hahn 2015).

Among all the flares observed in 2019 and 2020 (state F2), only P4 has good coverage of simultaneous multiwavelength data and hence provides an ideal situation to go for SED modelling. The other states like Q1 and F1 have very few observations in X-ray and optical/UV. The MW SEDs for states Q1 and F1 are also produced and their parameters are compared with the brightest state P4. GAMERA calculates the propagated electron spectrum for a given initial injected electron spectrum by solving the transport equation given in equation (3), and further estimates the synchrotron, synchrotron self-Compton (SSC), and inverse Compton (IC) emissions.

$$\frac{\partial N(E,t)}{\partial t} = Q(E,t) - \frac{\partial}{\partial E}(b(E,t)N(E,t)), \tag{3}$$

where *N*(*E*, *t*) is the propagated electron spectrum estimated at a time '*t*' for the initially injected electron spectrum (*Q*(*E*, *t*)). *b*(*E*, *t*) is dedicated to the radiative loss caused by physical processes, viz. synchrotron, SSC, and IC scattering. For the model fits here, we considered a single zone emission model with a log parabola electron distribution.

4.1 Jet parameters

Further, we tried to derive few jet parameters for this source based on our observational results. We can constrain the Doppler factor from the γ–γ opacity argument (Dondi & Ghisellini 1995; Ackermann et al. 2010) and which can be derived numerically by using the highest energy photon detected in γ-ray during the flare. The argument says that if the γ–γ interaction optical depth for the high energy photon is one, the minimum Doppler factor can be defined as

$$\delta_{\min} \cong \left[\frac{\sigma_T d_L^2 (1+z)^2 f_x \epsilon}{4 t_{\text{var}} m_e c^4}\right]^{1/6}, \tag{4}$$

where, σ_T is the Thompson scattering cross-section (6.65×10^{-25} cm^2), d_{L} is the luminosity distance (4.175 Gpc), f_x is the X-ray flux measured in the 0.3–10 keV (4.908×10^{-12} erg cm^{-2} s^{-1}), $\epsilon = E/m_e c^2$, E is the highest photon energy (∼77 GeV), and t_{var} is the observed variability time (9.01 ± 0.78 h). All the observed values are measured during the flare and are contemporaneous in nature. The Doppler factor derived from equation (4) is ∼12. In general, blazar has a similar bulk Lorentz and Doppler factor for the emitting blob, i.e. $\Gamma \sim \delta$ and which can provide the upper limit on the viewing angle of the jet, $\theta \le 1/\delta_{\min} = 4.8°$. The size and the location of the emission region can be constrained for the flaring period. The upper limit on size can be derived from the causality relation $R \sim c\ t_{\text{var}}\ \delta_{\min}/(1+z) \sim 6.94 \times 10^{15}$ cm. Assuming a conical jet scenario where the emission is produced across the entire jet area suggests the flaring site close to the central engine and the distance can be estimated as $d \sim 2\ c\ t_{\text{var}}\ \delta_{\min}^2/(1+z) \sim 0.05$ pc Abdo et al. (2011).

The total isotropic γ-ray luminosity can also be estimated for all the spectral shapes (PL, LP, PLEC, and BPL) by following the relation,

$$L_\gamma = 4\pi D_L^2 \int_{E_{\min}}^{E_{\max}} E \frac{\mathrm{d}N}{\mathrm{d}E} \mathrm{d}E, \tag{5}$$

where $E_{\min}$ is the lower energy range of *Fermi*–LAT (i.e. 100 MeV) and $E_{\max}$ is the energy of the highest photon detected during a particular period, d*N*/d*E* represents the various spectral models and D_{L} is the luminosity distance (4.259 Gpc). The γ-ray luminosity corresponding to each spectral models in their various states are shown in Table 4. The obtained values suggest that the γ-ray luminosity is more during the higher states P1, P2, P3, and P4 compared to the Q1 and F1 states.

4.2 External seed photons

In the leptonic scenario, BLR is believed to be the main source of seed photons that get up-scatted in the jet through the IC scattering and produces the high energy peak of the SED. Considering BLR as a thin spherical shell, makes easy to estimate the size of the BLR (Ghisellini

---

[5] http://joachimhahn.github.io/GAMERA

& Tavecchio 2009) and which can be scaled as, $R_{\rm BLR} = 10^{17}\, {\rm L}_{d,45}^{1/2}$, where $L_{d,45}$ is the disc luminosity in units of 10^{45} erg s^{-1}. The disc luminosity and mass of the SMBH for this source are estimated by Brotherton, Singh & Runnoe (2015), and the values are $M_{\rm SMBH} = 3.98 \times 10^8\, {\rm M}_{\odot}$ and $L_{\rm disc} = 9.2 \times 10^{45}$ erg s^{-1} after bolometric correction from Netzer (2019). After using the above value of $L_{\rm disc}$ the $R_{\rm BLR}$ is derived as 3.03×10^{17} cm ~ 0.1 pc. Comparing the $R_{\rm BLR}$ with the location of the emission region (∼0.05 pc), we conclude that the emission region is located at the inner boundary of the BLR. In our SED modelling we considered that the emission site is located within the BLR and the BLR plays an important role to produce the high energy peak of the SED. For our modelling purpose, we estimated the BLR photon energy density in the comoving frame by,

$$U^{'}_{\rm BLR} = \frac{\Gamma^2 \eta_{\rm BLR} L_{\rm disc}}{4\pi c R^2_{\rm BLR}}, \tag{6}$$

where the $\eta_{\rm BLR}$ is the fraction of disc emission processed in BLR, and typically it is around 10 per cent, and c is the speed of light in vacuum.

The contribution of direct disc emission as seed photons for IC scattering cannot be ignored and hence we also estimated the accretion disc photon energy density in the comoving frame from Dermer & Menon (2009),

$$U^{\prime}_{\rm disc} = \frac{0.207 R_g l_{\rm Edd} L_{\rm Edd}}{\pi c z^3 \Gamma^2}, \tag{7}$$

where, $R_{\rm g}$, $l_{\rm Edd} = L_{\rm disc}/L_{\rm Edd}$, and z are the gravitational radius, the Eddington ratio, and the location of the emission site from the SMBH, respectively. The gravitational radius is found to be $R_{\rm g} = 5.87 \times 10^{13}$ cm for the black hole mass $3.98 \times 10^8\, {\rm M}_{\odot}$. We did not consider dusty torus as a source of external photon field since there is no observational evidence. However, the dusty torus contribution could be important if the emission site is outside the BLR.

The calculated photon energy density in BLR and disc along with the BLR temperature (10^4 K; Peterson 2006) and disc temperature (1.1×10^5 K; estimated from Eddington ratio and BH mass; Panda et al. 2018) were fixed as inputs in GAMERA, and the parameters of the input injected electron distributions were kept free while modelling the multiwavelength SED. The size of the emitting blob was fixed from the variability time calculation, and the jet magnetic field was set free to obtain the good fit value of the multiwavelength SED.

4.3 Modelling results

We carried out the SED modelling for the states Q1, F1, and the high state P4, and the multiwavelength SED modelling plots are shown in Fig. 10. The best-fitting model parameters for SED modelling are shown in Table 5. The low energy peak is successfully constrained by the Synchrotron process and the γ-ray high energy peak with the IC process. The SSC mechanism well describes the X-ray emission in the high state P4, whereas in Q1 and F1 it is explained by external Compton process. The size of the emission region is found to be a bit more from the modelling than the estimated value from the variability time. The magnetic field in the blob is very much similar to the other FSRQ-type blazars like PKS 1510–089 (Prince, Gupta & Nalewajko 2019), 3C 279 (Prince 2020), 3C 454.3 (Das, Prince & Gupta 2020) etc. The Doppler factor and the Lorentz factor were optimized to 20 and 15.5 to obtain the best fit to the multiwavelength SED.

We also used the derived parameters to estimate the individual jet power in electrons, magnetic field, and protons. The total jet power can be defined as,

$$P_{\rm jet} = \pi r^2 \Gamma^2 c (U_e + U_B + U_P), \tag{8}$$

where, U_e, U_B, and U_P are the energy density in electrons, magnetic field, and protons. The size of the emitting zone and its Lorentz factor is denoted by r and Γ. The jet is considered as plasma of leptons and protons with the ratio of 20:1. The total jet power calculated here is always lesser than the total Eddington luminosity of the source. The power calculated for individual components are mentioned in Table 5. Comparing with the other flaring blazars like PKS 1510–089 (Prince et al. 2019), 3C 279 (Prince 2020), and 3C 454.3 (Das et al. 2020) the total and individual components powers are in good agreement. A blazar sample has been studied by Ghisellini & Tavecchio (2015), and they found that most of the blazars in their sample have $L_{\rm disc}/L_{\rm Edd} = 0.1$ and using this ratio the Eddington luminosity estimated in our case is 9.2×10^{46} erg s^{-1}, which is much greater than the total jet power estimated here. As we can see in Table 5, the total jet power is dominated by the magnetic field and hence powers the blazar, whereas both the leptons and protons power do not provide sufficient power and are unable to supply the energy to the radio lobes. Comparing the values obtained during various states suggest that more electrons and protons power are needed to transit the source from state Q1 to F1 and P4. Surprisingly the magnetic field and magnetic power obtained during state Q1 is more compared to state F1 and P4. A large value of minimum and maximum energy is required in electrons to make the source transit from low state (Q1) to high state (F1 and P4).

5 RESULTS: FLUX DISTRIBUTION OF OQ 334

Analysis of the γ-ray light curves, suggest that many blazars show lognormal behaviour in their flux distributions (Ackermann et al. 2015; Romoli et al. 2018; Shah et al. 2018). Among blazars, such lognormal behaviour was first detected in BL Lac, from RXTE observation (Giebels & Degrange 2009), later it was observed in many blazars at various energy bands and time-scales (H.E.S.S. Collaboration 2010; Tluczykont et al. 2010; Kushwaha et al. 2016; Sinha et al. 2016, 2017, 2018; Khatoon et al. 2020). Lognormal flux distributions were initially found in the X-ray emission of black hole binary Cygnus X-1 (Uttley & McHardy 2001; Quilligan et al. 2002; Giebels & Degrange 2009), and are generally explained by the fluctuations in the accretion disc, which imply multiplicative processes (Uttley, McHardy & Vaughan 2005; McHardy 2010). However, fast (minute time-scale) variability in the blazars' light curves, is difficult to produce in the disc (Narayan & Piran 2012), and supports to originate in the jet. Biteau & Giebels (2012) have shown that lognormal flux distribution can be explained by the multiplicative processes, however, according to Scargle (2020) lognormality of measured flux values need not imply multiplicative process. On the other hand, Gaussian perturbation in the particle acceleration time-scale is capable of producing a lognormal flux distribution (Sinha et al. 2018).

We studied the flux distribution property for the source OQ334, using three days binned γ-ray flux light curve. To select light curve with good statistics, we considered flux points for which TS>= 9, and also the flux points detected at greater than 2-σ level, such that $\frac{F}{\Delta F} > 2$. We performed Anderson–Darling (AD) test, where null hypothesis probability value (p-value) < 0.01 would indicate non-Gaussianity of the data. AD test results show that the test statistics (r) and p-value for flux in linear scale are 15.06 and 1.5×10^{-3}, while r-value and p-value for the flux in log-scale are 0.57 and 0.13, respectively, which implies that the flux distribution is

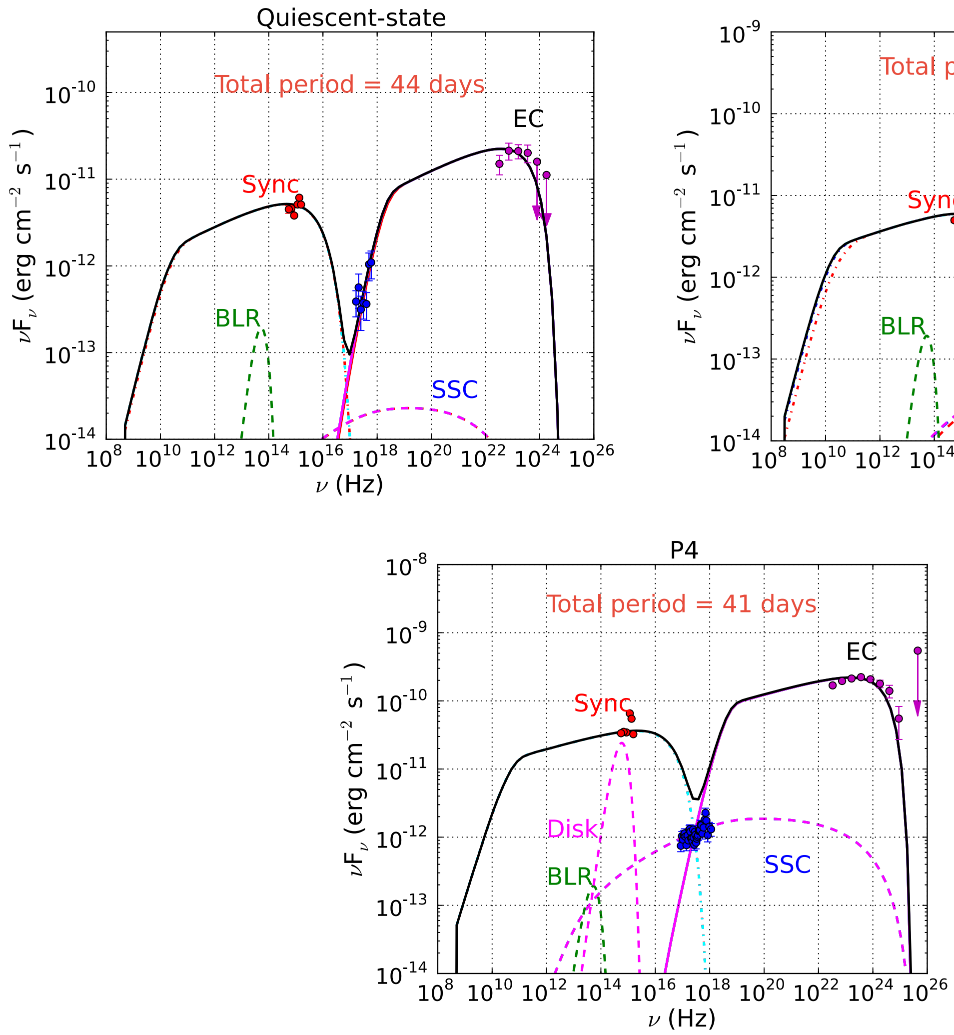

Figure 10. Multiwavelength SED of states Q1, F1, and the high state P4.

lognormal. To quantify this, we further fit the normalized histogram of the logarithm of flux with the Gaussian and lognormal probability density functions (PDFs) (Fig. 11), these PDFs are shown by Shah et al. (2018). We found that the lognormal PDF significantly fits the distribution better with reduced chi-square, $\chi^2_{\rm red} \approx 0.93$ for 8 degrees of freedom (dof), than the Gaussian PDF ($\chi^2_{\rm red} \approx 2.80$ for 8 dof). We further investigated the linear dependence of the average flux on its excess variance, which is an important feature for lognormal behaviour. For that purpose, we considered the Poisson noise corrected excess variance as given by, $\sigma_{XS} = \sqrt{S^2 - \overline{\sigma^2_{\rm err}}}$; where S^2 is the sample variance and $\overline{\sigma^2_{\rm err}}$ represents the mean of the square of the measurement errors (Vaughan et al. 2003). The flux-rms plot is shown in Fig. 12, where data are binned for a period of 50 d to obtain sufficient statistics. The scatter plot is well fitted by a linear function with slope 0.43 ± 0.05. Furthermore, we computed the Spearman's rank correlation coefficient (r_s) and the correlation probability (prob). The values of r_s and prob are found as 0.76 and 2.6×10^{-3}, indicating a strong correlation between flux and excess variance. The observed lognormal behaviour in the flux distribution and the proportionality between the average amplitude of variability to the flux, suggest that the variation in flux is lognormal.

6 SUMMARY

In this work, we present the first time detailed analysis of the γ-ray spectral and temporal behaviour as well as the broad-band SED modelling of the FSRQ OQ 334. We summarize the main results below,

(i) The source was faint in the γ-ray band for about 10 yr. It showed a bright γ-ray flare during 2017, returned back to the low brightness state, stayed in the low brightness state for few months and again moved to the higher γ-ray brightness state. Supermimposed on the high brightness state many small flares were observed, with the brightest γ-ray flare occurring in 2020 February. Thus the source has shown more than one episode of flaring activity in the γ-ray band between 2017 and 2020.

(ii) During various brightness state of the source such as P1, P2, P3, and P4 states, no correlation of the γ-ray photon index with the total flux of the source was found.

(iii) During most of the γ-ray brightness sates of the source, the γ-ray spectrum was well fit by a PLEC spectral model.

(iv) We found a time lag between the γ-ray and radio band light curve at the 2σ significance level with the radio variation leading variations in the γ-ray band by 70 d. The two emission regions are thus separated by ~11 pc.

Table 5. Multiwavelength SED modelling results with the best-fitting parameters values. The input injected electron distribution is LogParabola with reference energy 60 MeV.

High state	Parameters	Symbols	Values	Period
	BLR photon density	$U'_{\rm BLR}$	3.83 erg cm^{-3}	–
	BLR temperature	$T'_{\rm BLR}$	1.0×10^4 K	–
	Disc photon density	$U'_{\rm disc}$	2.21×10^{-6} erg cm^{-3}	–
	Disc temperature	$T'_{\rm disc}$	1.0×10^6 K	–
	Size of the emitting zone	R	2.6×10^{16} cm	–
	Doppler factor of the emitting zone	δ	20.0	–
	Lorentz factor of the emitting zone	Γ	15.5	–
Q1				44 d
	Min Lorentz factor of emitting electrons	$\gamma_{\rm min}$	5.0	–
	Max Lorentz factor of emitting electrons	$\gamma_{\rm max}$	6.3×10^3	–
	Input injected electron spectrum (LP)	α	1.68	–
	Curvature parameter of the PL spectrum	β	0.005	–
	Magnetic field in emitting zone	B	4.7 G	–
	Jet power in electrons	$P_{j,e}$	4.66×10^{44} erg s^{-1}	–
	Jet power in magnetic field	$P_{j,B}$	1.29×10^{46} erg s^{-1}	–
	Jet power in protons	$P_{j,P}$	4.35×10^{44} erg s^{-1}	–
	Total jet power	$P_{\rm jet}$	1.37×10^{46} erg s^{-1}	–
F1				25 d
	Min Lorentz factor of emitting electrons	$\gamma_{\rm min}$	5.0	–
	Max Lorentz factor of emitting electrons	$\gamma_{\rm max}$	1.1×10^4	–
	Input injected electron spectrum (LP)	α	1.77	–
	Curvature parameter of the PL spectrum	β	0.005	–
	Magnetic field in emitting zone	B	3.0 G	–
	Jet power in electrons	$P_{j,e}$	1.30×10^{45} erg s^{-1}	–
	Jet power in magnetic field	$P_{j,B}$	5.48×10^{45} erg s^{-1}	–
	Jet power in protons	$P_{j,P}$	1.20×10^{45} erg s^{-1}	–
	Total jet power	$P_{\rm jet}$	7.98×10^{45} erg s^{-1}	–
P4				41 d
	Min Lorentz factor of emitting electrons	$\gamma_{\rm min}$	8.0	–
	Max Lorentz factor of emitting electrons	$\gamma_{\rm max}$	1.6×10^4	–
	Input injected electron spectrum (LP)	α	1.77	–
	Curvature parameter of the PL spectrum	β	0.005	–
	Magnetic field in emitting zone	B	3.9 G	–
	Jet power in electrons	$P_{j,e}$	4.84×10^{45} erg s^{-1}	–
	Jet power in magnetic field	$P_{j,B}$	9.26×10^{45} erg s^{-1}	–
	Jet power in protons	$P_{j,P}$	3.43×10^{45} erg s^{-1}	–
	Total jet power	$P_{\rm jet}$	1.75×10^{46} erg s^{-1}	–

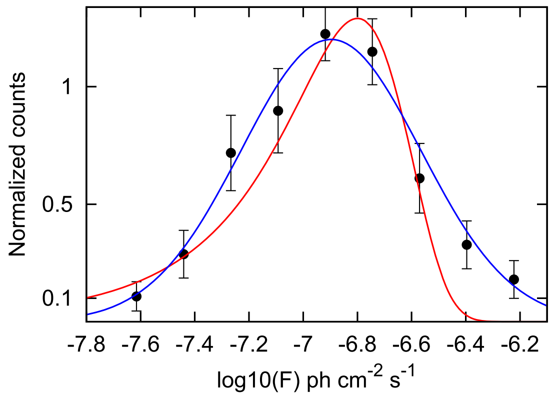

Figure 11. Histogram of the logarithm of 3 d binned γ-ray fluxes. The red and blue lines represent the Gaussian and lognormal PDFs, respectively.

(v) We found the fastest variability time on scales of 9.01 ± 0.78 h. Using that we constrained the size and location of the emission region as 6.95×10^{15} cm and 0.05 pc, respectively.

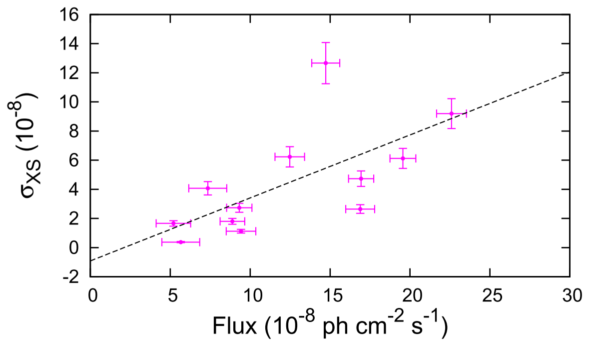

Figure 12. Excess variance versus mean flux scatter plot, with the best-fitting line (black).

(vi) The broad-band SED modelling indicates that the location of the γ-ray emission region is inside the BLR. The observed γ-ray emission during Q1, F1, and P4 states are the combination of SSC and IC scattering. The physical parameters obtained from SED modelling indicates that more electron and proton power are needed to transit the source from Q1 to F1 and further in P4 state.

(vii) The flux distribution shows the lognormal behaviour in the source.

ACKNOWLEDGEMENTS

We thank the referee for providing stimulating comments in order to improve the paper. The project was partially supported by the Polish Funding Agency National Science Centre, project 2017/26/A/ST9/00756 (MAESTRO 9), and MNiSW grant DIR/WK/2018/12. RP thanks Avik Kumar Das for SED modelling discussions. RP thanks Prof. Bożena Czerny, Swayamtrupta Panda, and Michal Zajacek for discussions. This work has made use of public *Fermi* data obtained from FSSC. This research has also made use of XRT data analysis software (XRTDAS) developed by ASI science data center, Italy. This research has made use of radio data from OVRO 40-m monitoring programme (Richards et al. 2011) which is supported in part by NASA grants NNX08AW31G, NNX11A043G, and NNX14AQ89G and NSF grants AST-0808050 and AST-1109911.

DATA AVAILABILITY

This research has made use of archival data from various sources e.g. *Fermi*, *Swift*, and OVRO observatory and their proper links are given in the manuscript. All the models and softwares used in this manuscript are also publicly available.

REFERENCES

Abdo A. A. et al., 2010, ApJ, 722, 520
Abdo A. A. et al., 2011, ApJ, 733, L26
Abdollahi S. et al., 2020, ApJS, 247, 33
Ackermann M. et al., 2010, ApJ, 716, 1178
Ackermann M. et al., 2015, ApJ, 810, 14
Angioni R., 2019, Astron. Telegram, 12942, 1
Arnaud K. A., 1996, in Jacoby G. H., Barnes J., eds, ASP Conf. Ser. Vol. 101, Astronomical Data Analysis Software and Systems V. Astron. Soc. Pac., San Francisco, p. 17
Atwood W. B. et al., 2009, ApJ, 697, 1071
B"ottcher M., Reimer A., Sweeney K., Prakash A., 2013, ApJ, 768, 54
Banik P., Bhadra A., Bhattacharyya A., 2020, MNRAS, 500, 1087
Biteau J., Giebels B., 2012, A&A, 548, A123
Blandford R. D., Königl A., 1979, ApJ, 232, 34
Blandford R. D., Levinson A., 1995, ApJ, 441, 79
Breeveld A. A., Landsman W., Holland S. T., Roming P., Kuin N. P. M., Page M. J., 2011, in McEnery J. E., Racusin J. L., Gehrels N., eds, AIP Conf. Proc. Vol. 1358, American Institute of Physics Conference Series. Am. Inst. Phys., New York, p. 373
Britzen S., Fendt C., Zajaček M., Jaron F., Pashchenko I., Aller M. F., Aller H. D., 2019, Galaxies, 7, 72
Brotherton M. S., Singh V., Runnoe J., 2015, MNRAS, 454, 3864
Cerruti M., 2020, Galaxies, 8, 72
Cerruti M., Zech A., Boisson C., Emery G., Inoue S., Lenain J. P., 2019, MNRAS, 483, L12
Chatterjee R. et al., 2012, ApJ, 749, 191
Ciprini S., 2018, Astron. Telegram, 12277, 1
Ciprini S., Cheung C. C., 2020, Astron. Telegram, 13382, 1
Connolly S. D., 2016, DELightcurveSimulation: Light curve simulation code, record ascl:1602.012
Costamante L., Cutini S., Tosti G., Antolini E., Tramacere A., 2018, MNRAS, 477, 4749
Das A. K., Prince R., Gupta N., 2020, ApJS, 248, 8
Dermer C. D., Menon G., 2009, High Energy Radiation from Black Holes: Gamma Rays, Cosmic Rays, and Neutrinos. Princeton Univ. Press, Princeton, NJ
Dermer C. D., Schlickeiser R., 1994, ApJS, 90, 945
Dermer C. D., Schlickeiser R., Mastichiadis A., 1992, A&A, 256, L27
Dondi L., Ghisellini G., 1995, MNRAS, 273, 583
Edelson R. A., Krolik J. H., 1988, ApJ, 333, 646
Emmanoulopoulos D., McHardy I. M., Papadakis I. E., 2013, MNRAS, 433, 907
Ghisellini G., Madau P., 1996, MNRAS, 280, 67
Ghisellini G., Tavecchio F., 2009, MNRAS, 397, 985
Ghisellini G., Tavecchio F., 2015, MNRAS, 448, 1060
Giebels B., Degrange B., 2009, A&A, 503, 797
Goyal A., 2020, MNRAS, 494, 3432
Goyal A. et al., 2017, ApJ, 837, 127
Goyal A. et al., 2018, ApJ, 863, 175
H.E.S.S. Collaboration, 2010, A&A, 520, A83
Hahn J., 2015, Proc. Sci., GAMERA - A New Modeling Package for Non-thermal Spectral Modeling. SISSA, Trieste, PoS(ICRC2015)917
Hartman R. C. et al., 1999, ApJS, 123, 79
Heidt J., Wagner S. J., 1996, A&A, 305, 42
Hewett P. C., Wild V., 2010, MNRAS, 405, 2302
Hovatta T., Lindfors E., 2019, New Astron. Rev., 87, 101541
IceCube Collaboration, 2018, Science, 361, eaat1378
Kalberla P. M. W., Burton W. B., Hartmann D., Arnal E. M., Bajaja E., Morras R., Pöppel W. G. L., 2005, A&A, 440, 775
Khatoon R., Shah Z., Misra R., Gogoi R., 2020, MNRAS, 491, 1934
Kushwaha P., Chandra S., Misra R., Sahayanathan S., Singh K. P., Baliyan K. S., 2016, ApJ, 822, L13
Larionov V. M. et al., 2016, MNRAS, 461, 3047
Liodakis I. et al., 2017, MNRAS, 466, 4625
Liu H. T., Bai J. M., 2006, ApJ, 653, 1089
Lynden-Bell D., 1969, Nature, 223, 690
Mattox J. R. et al., 1996, ApJ, 461, 396
Max-Moerbeck W. et al., 2014, MNRAS, 445, 428
McHardy I., 2010, in Belloni T., ed., Lecture Notes in Physics, Vol. 794. Springer-Verlag, Berlin, p. 203
Narayan R., Piran T., 2012, MNRAS, 420, 604
Netzer H., 2019, MNRAS, 488, 5185
Nolan P. L. et al., 2012, ApJS, 199, 31
Paliya V. S., Sahayanathan S., Stalin C. S., 2015, ApJ, 803, 15
Paliya V. S., Diltz C., B"ottcher M., Stalin C. S., Buckley D., 2016, ApJ, 817, 61
Panda S., Czerny B., Adhikari T. P., Hryniewicz K., Wildy C., Kuraszkiewicz J., Śniegowska M., 2018, ApJ, 866, 115
Peterson B. M., 2006, in Alloin D., Johnson R., Lira P., eds, Lecture Notes in Physics, Vol. 693, Physics of Active Galactic Nuclei at all Scales. The Broad-Line Region in Active Galactic Nuclei. Springer, Berlin, Heidelberg, p. 77
Prince R., 2019, ApJ, 871, 101
Prince R., 2020, ApJ, 890, 164
Prince R., Raman G., Hahn J., Gupta N., Majumdar P., 2018, ApJ, 866, 16
Prince R., Gupta N., Nalewajko K., 2019, ApJ, 883, 137
Quilligan F., McBreen B., Hanlon L., McBreen S., Hurley K. J., Watson D., 2002, A&A, 385, 377
Rajput B., Stalin C. S., Sahayanathan S., Rakshit S., Mandal A. K., 2019, MNRAS, 486, 1781
Rajput B., Stalin C. S., Sahayanathan S., 2020, MNRAS, 498, 5128
Richards J. L. et al., 2011, ApJS, 194, 29
Roming P. W. A. et al., 2005, Space Sci. Rev., 120, 95
Romoli C., Chakraborty N., Dorner D., Taylor A., Blank M., 2018, Galaxies, 6, 135
Scargle J. D., 2020, ApJ, 895, 90
Schlafly E. F., Finkbeiner D. P., 2011, ApJ, 737, 103
Shah Z., Mankuzhiyil N., Sinha A., Misra R., Sahayanathan S., Iqbal N., 2018, Res. Astron. Astrophys., 18, 141
Sikora M., Begelman M. C., Rees M. J., 1994, ApJ, 421, 153

Sikora M., Stawarz Ł., Moderski R., Nalewajko K., Madejski G. M., 2009, ApJ, 704, 38
Sinha A. et al., 2016, A&A, 591, A83
Sinha A., Sahayanathan S., Acharya B. S., Anupama G. C., Chitnis V. R., Singh B. B., 2017, ApJ, 836, 83
Sinha A., Khatoon R., Misra R., Sahayanathan S., Mandal S., Gogoi R., Bhatt N., 2018, MNRAS, 480, L116
Tluczykont M., Bernardini E., Satalecka K., Clavero R., Shayduk M., Kalekin O., 2010, A&A, 524, A48
Ulrich M.-H., Maraschi L., Urry C. M., 1997, ARA&A, 35, 445
Urry C. M., Padovani P., 1995, PASP, 107, 803
Uttley P., McHardy I. M., 2001, MNRAS, 323, L26
Uttley P., McHardy I. M., Vaughan S., 2005, MNRAS, 359, 345
Vaughan S., Edelson R., Warwick R. S., Uttley P., 2003, MNRAS, 345, 1271

This paper has been typeset from a TEX/LATEX file prepared by the author.